Ceramics International 51 (2025) 46891–46902

Contents lists available at ScienceDirect

Ceramics International

journal homepage: www.elsevier.com/locate/ceramint

Surface and structural changes in SiC pre-implanted with helium, silver, and strontium after annealing, and their effect on silver and strontium migration

G. Ntshobeni [a,*], Z.A.Y. Abdalla [a], H.A.A. Abdelbagi [b], A. Sohatsky [c], T. Nguyen [c,d], E.G. Njoroge [a,e], V.A. Skuratov [c,f,g], M. Mlambo [h], T.T. Hlatshwayo [a]

[a] Physics Department, University of Pretoria, Pretoria, South Africa
[b] Physics Department, University of Zululand, KwaDlangezwa, South Africa
[c] Joint Institute for Nuclear Research, Dubna, Russia
[d] Institute of Physics, Vietnam Academy of Science and Technology, Hanoi City, 100000, Viet Nam
[e] ENGAGE, University of Pretoria, Pretoria, 0002, South Africa
[f] Dubna State University, Dubna, Moscow Region, Russia
[g] National Research Nuclear University MEPhI, Moscow, Russia
[h] Department of Biotechnology and Chemistry, Vaal University of Technology, Vanderbijlpark, 1900, South Africa

ARTICLE INFO

Handling Editor: Dr P. Vincenzini

Keywords:
SiC
He implantation
Recrystallization
Migration
Deep voids/holes

ABSTRACT

The effect of helium (He), silver (Ag) and strontium (Sr) ions implantation and annealing on the surface and structural properties of SiC as well as the migration of Ag and Sr was investigated in this study. Ag and Sr were sequentially implanted at 360 keV and 280 keV, respectively, each to a fluence of 2×10^{16} cm^{-2} at 600 °C. Some dual implanted (Ag + Sr-SiC) samples were additionally implanted with He of 17 keV to a 1×10^{17} cm^{-2} at 350 °C, forming triple-implanted samples (Ag + Sr + He-SiC). Both dual and triple implanted samples underwent isochronal annealing at 1100, 1200, and 1300 °C for 5 h. Ag, Sr and He implantation introduced defects in both dual and triple implanted samples. However, triple-implanted samples developed surface blisters and holes due to the migration of He bubbles. At 1100 °C, partial recovery of structural damage was observed in both dual- and triple-implanted samples, but graphite formed in the latter, and holes persisted. At higher temperatures (i.e., 1200 and 1300 °C), dual-implanted samples showed significant structural recovery, whereas the graphite in triple-implanted samples impeded the healing of defects. Depth profiling revealed minimal changes in Ag and Sr distributions and concentrations in dual-implanted samples post-annealing up to 1300 °C. However, triple-implanted samples lost ~20 % of Ag and Sr at 1100 °C due to sublimation via holes. At 1200 and 1300 °C, no further losses occurred, but Ag and Sr migrated toward the surface. These findings suggest that He implantation promotes the formation of holes in SiC, facilitating the loss of Ag and Sr at 1100 °C. Additionally, He-induced defects enhance the migration of Ag and Sr toward the surface during annealing at 1200 and 1300 °C.

1. Introduction

Nuclear fuels used in modern reactors are designed to contain fission products (FPs) within the fuel structure during normal reactor operation and in the event of accidents [1,2], such as the Three Mile Island and Fukushima incidents. Tri-structural isotropic (TRISO) particles are one of the efficient nuclear fuels used in Pebble Bed Modular Reactors (PBMRs) [3,4]. A TRISO particle is composed of uranium dioxide (UO_2) as a kernel surrounded by four layers, namely a porous carbon buffer layer, an inner pyrolytic carbon layer, a silicon carbide (SiC) layer, and an outer pyrolytic carbon layer. Among these layers, SiC serves as the primary diffusion barrier for fission products (FPs) due to its unique properties, such as excellent chemical resistance, high durability, low thermal expansion, low neutron cross section and high thermal conductivity [3]. Chemical vapor deposition (CVD) is used to grow the polycrystalline SiC layer in TRISO fuel particles and is selected in such a way that the crystals consist primarily of 3C, the preferred polycrystalline type for nuclear reactors. This 3C polytype is preferred in

* Corresponding author.
E-mail address: gcobani636@gmail.com (G. Ntshobeni).

https://doi.org/10.1016/j.ceramint.2025.07.393
Received 17 May 2025; Received in revised form 9 July 2025; Accepted 28 July 2025
Available online 31 July 2025

nuclear reactor applications, primarily due to its superior resistance to neutron-induced defect formation compared to α-SiC [5]. While TRISO particles are effective at retaining most of the FPs during normal reactor operating temperatures (i.e., 950 °C), some FPs, such as silver (Ag), strontium (Sr), xenon (Xe), and europium (Eu), have been found to escape from the fuel particle structure [6].

The release of FPs such as Ag and Sr into the environment poses significant ecological and health risks due to their radioactive properties. Ag, with a half-life of 249.8 days, is a strong gamma emitter and can contaminate soil and water. Sr, a beta emitter with a half-life of 28.9 years, is particularly hazardous because it mimics calcium, accumulating in bones and teeth, thus increasing the risk of bone cancer and leukemia. To enhance the durability of TRISO particles in retaining Ag and Sr FPs, it is crucial to understand the migration behavior of these FPs in SiC, which serves as the primary barrier to FPs.

Extensive studies have been conducted to explain the transport mechanisms of Ag and Sr in SiC, including out-of-pile release measurements from irradiated TRISO fuel [3,7–10], as well as ion implantation and annealing experiments [3, 11–16]. Using ion implantation methods, Ag and Sr were implanted separately into SiCat temperatures between room temperature (RT) and 600 °C, all to a fluence of 2×10^{16} cm^{-2} and subsequently annealed at temperatures ranging from 1000 to 1500 °C [3,11–16]. According to these studies, annealing RT implanted samples caused significant diffusion of Ag (from 1100 °C upwards) and Sr (from 1000 °C upwards), while slight migration was observed in samples implanted at temperatures higher than 350 °C annealed under the same conditions. The explanation for this discrepancy lies in the initial amount of radiation damage in SiC. Samples implanted at RT exhibited more damage/defects, which enhanced Ag and Sr migration. In contrast, samples implanted at temperatures above 350 °C had less radiation damage, leading to less migration of implanted species.

Other studies have investigated the synergistic effect of FP surrogates on the migration behavior of Ag implanted into SiC [17–20]. Ag implanted samples were co-implanted separately with palladium (Pd) [18], iodine (I) [19], ruthenium (Ru) [20] and Sr [17] followed by annealing at temperatures ≥1000 °C. Iodine was found to assist in Ag retention within SiC [19], while Pd and Ru were found to facilitate Ag migration [18,20]. On the other hand, annealing Ag and Sr co-implanted samples caused shifts in the depth profiles of Ag and Sr toward the surface that accompanied by the loss of Ag and Sr concentrations [17]. This loss was found to be due to Ag interacting with SiC resulting in the formation of deeper holes that act as migration channels. The findings suggest that Ag plays a critical role in the observed loss of implanted Sr.

Quite recent studies have investigated the migration of some FPs (such as Ag, and Sr) co-implanted with helium (He) in SiC [21–26] and krypton (Kr) [27]. The motivation for such studies was that He and Kr gases are generated in the reactor environment due to the emission of α-particles from nuclear reactions as well as from nuclear transmutation [28] and as FPs. In these studies [21–26], Sr and Ag were implanted separately into two different samples and subsequently implanted with He and annealed at high temperatures (≥1000 °C). These cavities were found to trap Ag and Sr atoms from migrating in SiC [21,22]. On the other hand, the exfoliation of He bubbles created holes on the SiC surface which enhanced the escape of Ag and Sr atoms from the SiC substrate [21,22]. Moreover, no similar holes were reported in SiC samples co-implanted with Kr and Ag and annealed at 1500 °C [27]. However, Kr cavities were found to enhance Ag diffusion in SiC. The lack of surface exfoliation in Kr-implanted samples suggests that Kr cavities enhance Ag transport within the substrate but do not promote Ag escape, resulting in a more contained redistribution of Ag compared to those implanted with He.

To date, only a one study has explored the role of He in the migration of Ag and Sr co-implanted into SiC [29]. In this previous study, the migration of Ag and Sr co-implanted into SiC was investigated in the presence and absence of He atoms after annealing at 1000 °C for 5 h [29]. The results indicated that there was neither migration nor loss of the implanted species in the dual-implanted (Ag + Sr–SiC) samples annealed at 1000 °C. In contrast, annealing the triple-implanted (Ag + Sr + He-SiC) samples led to a slight diffusion of Ag and Sr and a limited reduction in their concentrations. This suggests that He slightly facilitates the migration of Ag and Sr at 1000 °C, a temperature close to the reactor operating temperature (approximately 950 °C). However, since TRISO particles are designed to retain FPs within their structure during normal operation and accident conditions, it is crucial to investigate the effect of He on the migration of Ag and Sr in SiC at higher temperatures (>1000 °C), similar to those encountered during accident conditions. This study investigates the effects of high temperatures (1100 °C, 1200 °C and 1300 °C) on the surface and structural properties of SiC pre-implanted with Ag, Sr, and He, as well as the migration behavior of the implanted FPs surrogates (i.e., Ag and Sr).

2. Experimental procedure

Polycrystalline SiC wafers from Valley Design Corporation were used in this study. The as-received SiC samples were characterized by X-ray diffraction (XRD), scanning electron microscopy (SEM) and electron backscatter diffraction (EBSD) [13]. From these measurements, SiC crystallites were found to be primarily cubic (3C–SiC), with some hexagonal features (6H–SiC). SiC wafers were implanted with 360 keV Ag ions to a fluence of 2×10^{16} cm^{-2} at 600 °C. Subsequently, the same samples were implanted with 280 keV Sr ions at the same fluence and temperature (i.e., 2×10^{16} cm^{-2} at 600 °C). Ag and Sr implantation was performed at the Friedrich-Schiller-University Jena, Germany. Moreover, some of the dual implanted (Ag + Sr–SiC) samples were implanted with He ions of 17 keV to a fluence of 1×10^{17} cm^{-2} at 350 °C. He implantation was performed at iThemba LABS, in South Africa. Moreover, Ag, Sr and He ions implantations were performed at temperatures ≥350 °C to prevent amorphization of the SiC structure, ensuring the material retains its crystalline integrity.

The dual and triple implanted samples were isochronally annealed under vacuum (10^{-5} Pa) using a computer-controlled Webb 77 graphite furnace. The samples were annealed at 1100, 1200 and 1300 °C for 5 h. The structural changes and surface modifications in the SiC substrates due to implantation and annealing were investigated by Raman spectroscopy, scanning transmission electron microscopy (STEM), scanning electron microscopy (SEM) and atomic force microscopy (AFM). Furthermore, Rutherford backscattering spectrometry (RBS) was used to study the migration of the implants (Ag and Sr) in the dual and triple implanted samples after annealing.

WITec alpha 300 confocal Raman spectroscopy instrument with a 100 × 0.9NA objective lens was used to acquire Raman spectra at a wavelength of 532 nm and a laser excitation power of 20 mW. In order to analyse the Raman spectra of the samples, the baseline of the spectrum was corrected using a linear background correction. In the OriginLab program [30], the Raman spectra were fitted using the Gaussian and the Breit-Wigner-Fano (BWF) functions to determine the width (i.e., full width at half maximum (FWHM)) of the peaks and their positions. Moreover, the penetration depth of the 532 nm laser in SiC was calculated by dividing the wavelength by the extinction coefficient, as shown in the following equation, $z = \lambda/4\pi k$, and found to be 100 nm.

For the STEM measurements, lamellae were prepared using the focused ion beam (FIB) technique - the FEI Helios NanoLab 650 Dual Beam system. To protect lamellae surfaces from damage during the thinning process by Ga ions, two platinum layers were sequentially deposited via electron and ion beam deposition. Thermoscientific Talos F200i field emission scanning transmission electron microscope (at the Joint Institute for Nuclear Research (JINR)) was used to conduct STEM and energy dispersive X-ray spectroscopy (EDX) elemental mapping at a voltage of 200 kV.

SEM was used to study the topography of SiC surfaces after implantation and annealing. A high-resolution Zeiss Gemini Ultra Plus 55 field emission scanning electron microscope (FE-SEM) operated at 2 kV

under vacuum was used in this study. In order to prevent electron scattering by residual gas molecules, the FE-SEM column was evacuated to 10^{-5} Torr using a mechanical pump.

AFM images were obtained using the Dimension Icon AFM system. A sharp nitride lever (SNL) probe with a tip radius of 2 nm, a spring constant of 0.30 N/m, and a scan rate of 0.3 Hz is used for this system, which operates in contact mode. The resonance frequency of the SNL probe was 40–75 kHz. To determine the surface roughness of all samples, AFM images were further analysed using NanoScope Analysis (Bruker, USA) [31,32].

RBS was performed on the as-implanted and annealed samples using a mono-energetic beam of 2 MeV alpha particles from the 3 MV Tandetron accelerator machine. The backscattered alpha (He) particles were detected using a silicon surface barrier detector (with 20 keV resolution) set at 150°, and a charge of 0.5 μC was collected per measurement. The beam spot size was approximately 2 mm while the pressure in the RBS chamber kept at 5×10^{-6} mbar. Moreover, to calibrate the channel positions, gold-cobalt on Si dioxide, deposited on Si substrate (i.e., $AuCo/SiO_2/Si$) was used as a standard sample. Based on Ziegler, Biersack, and Littmark (ZBL) stopping powers [33], Ag and Se profiles in energy channels were converted into depth profiles using a SiC density of 3.21 gcm^{-3}.

Prior to the implantation process, ion range and damage simulations were conducted to determine the appropriate implantation energies needed to achieve overlapping projected ranges in SiC. These simulations guided the selection of ion energies to ensure that the implanted species (Ag, Sr, and He) were localized within similar depths in the substrate. Fig. 1 presents the theoretical depth distributions and displacement per atom (dpa) values calculated using the SRIM 2013 software [33] for Ag ions at 360 keV, Sr at 280 keV, and He at 17 keV, all implanted into SiC. The simulations assumed a SiC density of 3.21 g/cm^3, and threshold displacement energies of 35 eV for silicon and 20 eV for carbon [34]. Considering a critical amorphization threshold of 0.3 dpa for SiC [35], these implantation conditions would typically lead to full amorphization at room temperature. However, since the implantations were conducted at elevated temperatures above the amorphization threshold [36] significant dynamic annealing was expected, reducing the likelihood of complete amorphization. As shown in Fig. 1(a), the Ag and Sr implants produced overlapping depth profiles centered around 120 nm below the surface. Ag implantation resulted in a peak damage of approximately 60 dpa, while Sr caused about 45 dpa, both peaking at depths near 90 nm. When combined, Ag and Sr ions generated a cumulative damage of around 106 dpa, centered at approximately 85 nm. Fig. 1(b) illustrates the He profile, showing a lower peak damage of about 5.3 dpa at a depth of 110 nm. Implantation of Ag, Sr, and He led to a combined damage peak of 110 dpa at 85 nm, with all three ions showing overlapping distributions. This spatial overlap allows a focused investigation into how He influences the migration behavior of Ag and Sr in the SiC.

3. Results and discussion

Fig. 2 shows the Raman spectra of dual-implanted (Ag + Sr–SiC, Fig. 2(a)) and triple-implanted (Ag + Sr + He-SiC–SiC, Fig. 2(b)) SiC samples, both before and after annealing, along with the un-implanted (virgin) SiC spectrum for comparison. The un-implanted spectrum shows sharp and well-resolved peaks at 766, 792, and 964 cm^{-1}. The peaks at 792 and 964 cm^{-1} correspond to the transverse optical (TO) and longitudinal optical (LO) signatures of 3C-SiC. Moreover, the peak located around 766 cm^{-1} represents the TO phonon mode of hexagonal polytype 6H-SiC [37], indicating that there is a small fraction of hexagonal polytypes in polycrystalline SiC. In addition, the low intense peaks at ~1515 cm^{-1} and ~1710 cm^{-1} correspond to second order peaks [26,37], which indicate SiC wafers of good crystalline quality.

After dual and triple implantation, the intensities of the characteristic peaks observed in the un-implanted SiC spectrum decreased significantly. Moreover, broad peaks in the ranges of 400–600 cm^{-1} and 1100–1700 cm^{-1} appeared, confirming the formation of Si–Si and C–C homonuclear bonds, respectively. Considering the high ion fluences of implanted Ag, Sr, and He, one might have expected the SiC to become fully amorphous. However, the lack of complete amorphization can be attributed to the implantation temperatures, which were higher than the critical temperature for amorphization (approximately 300 °C). Annealing the dual-implanted samples at temperatures ranging from 1100 °C to 1300 °C led to the partial removal of defects from SiC, as evidenced by the increase in the intensities of the peaks at 766, 792, and 964 cm^{-1}. However, Si–Si homonuclear bonds were still present even after annealing at 1300 °C, indicating the persistence of some defects within the recrystallized SiC. In contrast, annealing the triple-implanted samples at 1100 °C led to partial recovery, accompanied by the appearance of D and G peaks at 1346 cm^{-1} and 1587 cm^{-1}, respectively, along with Si–Si homonuclear bonds. This suggests that some carbon crystals formed in the triple-implanted samples after annealing, which may be related to the presence of He, as no similar features were observed in the dual-implanted samples annealed under the same conditions. Similar phenomena were observed by Mokgadi et al. [22] when SiC samples were co-implanted with Sr and He at room temperature, then annealed at 1000 °C. After annealing, He formed large bubbles, while Si and C interstitials migrated and agglomerated into clusters around the He bubbles, which could explain the strong D and G bands [20,21]. Further annealing at 1200 °C and 1300 °C resulted in progressive defect recovery in the triple-implanted samples, with the D and G peaks disappearing after annealing at 1300 °C (see Fig. 2(b)). Additionally, the intensity of the Si–Si peak decreased, indicating that C

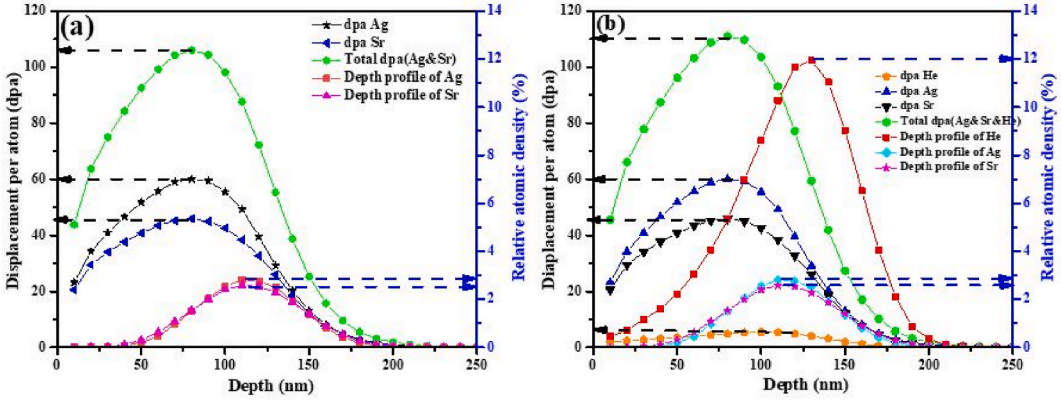

Fig. 1. Displacement per atom (dpa) and relative atomic density (%) as a function of depth, obtained from SRIM simulations, for (a) Ag and Sr, and (b) Ag, Sr and He implanted into SiC.

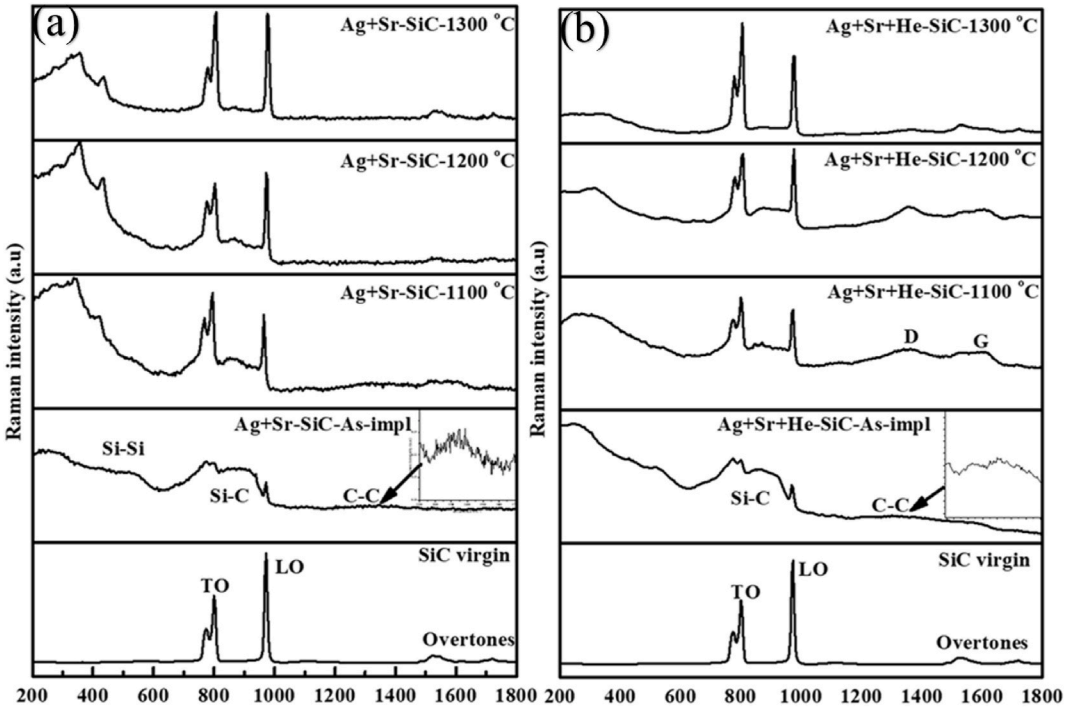

Fig. 2. Raman spectra of (a) dual, and (b) triple implantation before and after annealing at temperatures from 1100 to 1300 °C for 5 h. The spectrum of un-implanted SiC is included for comparisons.

atoms in graphite crystals were bonded to free Si atoms, resulting in enhanced SiC vibrations, as evidenced by the high TO intensity (and sharp LO peak) after annealing at 1300 °C.

The shift in the position of longitudinal optical (LO) peaks provides valuable information about residual stress in the SiC lattice [36]. A shift toward lower wavenumbers typically indicates the presence of tensile stress, which stretches the lattice, while a shift toward higher wavenumbers suggests compressive stress, which contracts the lattice [36]. In addition, the full width at half maximum (FWHM) of the LO peaks reflects the level of structural disorder or defect concentration within the SiC [36]. Broader peaks are associated with a higher density of defects such as vacancies, interstitials, or amorphous regions as these imperfections disrupt crystal periodicity and phonon coherence. Therefore, analyzing both the position and broadening of the LO peaks provides insight into the extent of damage and stress induced by ion implantation and the effectiveness of subsequent annealing processes in restoring crystallinity [36].

The origin of tensile stress in ion-implanted SiC can be attributed to the accumulation of He-induced defects in the crystal lattice [23]. When He ions are implanted into SiC, they do not chemically bond with either silicon or carbon atoms due to He's inert nature. Instead, they interact physically with the lattice, creating vacancies and interstitial defects. These He atoms may form vacancy-He or interstitial-He complexes. As the annealing temperature increases, the atoms tend to cluster in these defect-rich regions to form He bubbles, owing to their small atomic radius and low solubility in SiC. These bubbles can induce local swelling and cause internal pressure buildup within the lattice. This internal pressure leads to mechanical stress, which can manifest tensile stress when the lattice is locally expanded or distorted. Such stress conditions can influence defect dynamics and the migration of fission products in SiC.

Fig. 3 shows the Raman peak position and FWHM of the LO mode as a function of annealing temperature for dual (a) and triple (b) implanted SiC. The LO mode positions remained nearly unchanged in both as-implanted and annealed samples for both dual and triple implantations, indicating minimal tensile or compressive stresses in the Si-C bonds [36]. However, even minimal or undetectable shifts should be interpreted in light of the microstructural changes caused by He implantation, as localized stress fields may not be fully reflected in the Raman spectra. In contrast, the FWHM of the LO mode increased after

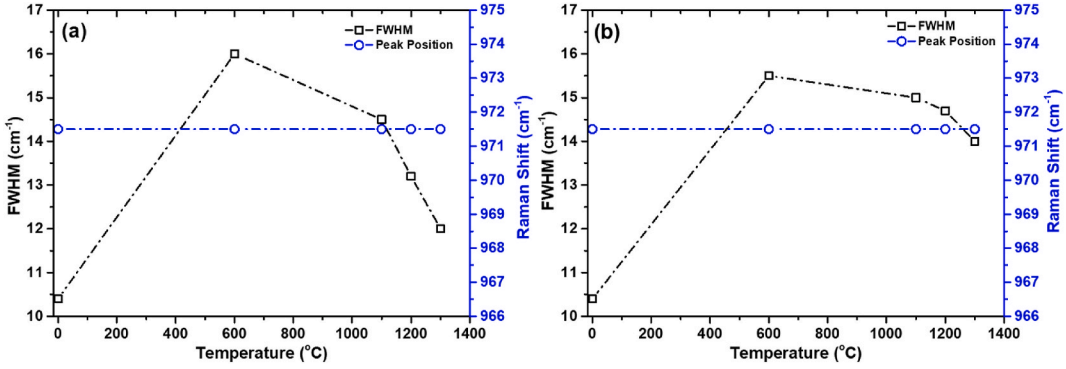

Fig. 3. The peak position and FWHM of the LO peak in dual (a) and triple samples (b) as a function of temperature.

implantation in both cases, with the dual-implanted samples showing a slightly broader peak. This suggests the presence of defects, with more defects retained in the dual-implanted SiC. The lower defect retention in the triple-implanted samples may be due to implantation temperature (i.e., that causes defect removal) or the high concentration of He, which can induce localized recrystallization [38].

Annealing reduces the FWHM of the LO peaks i.e., the peaks become narrower in both dual and triple implanted samples, indicating the removal of defects. This is further supported by the increase in LO peak intensities after annealing. Nevertheless, the FWHM values of samples annealed at 1300 °C remain higher than those of un-implanted SiC, suggesting that annealing does not completely remove the damage introduced by ion implantation. Interestingly, after annealing under the same conditions, the FWHM of dual-implanted samples is generally narrower than that of triple-implanted ones. This suggests that dual-implanted samples exhibit a greater degree of recovery. The reduced recovery in annealed triple-implanted SiC may be attributed to graphite crystals formation or He migration, which is known to form large bubbles within SiC after annealing. These bubbles can evolve into holes or craters (i.e., exfoliated blisters) in the surface layer, thereby limiting structural recovery [21,22].

Fig. 4 shows SEM micrographs of dual-implanted SiC samples before and after annealing, alongside a reference image of the un-implanted SiC surface. As shown in Fig. 4(a), the surface of the un-implanted sample exhibits distinct polishing marks linear grooves introduced during the mechanical surface preparation process. These features serve as a baseline for assessing the surface morphology changes due to ion implantation and subsequent thermal processing. After dual ion implantation, as seen in Fig. 4(b), the visibility of polishing marks significantly diminishes. This reduction in contrast and definition of surface features may result from surface erosion caused by high-energy ion bombardment, which can sputter away surface atoms and introduce localized roughening. Another contributing factor could be volumetric swelling of the SiC lattice due to defect accumulation and sub-surface damage, leading to decreased density and smoothing of surface relief features [29]. Importantly, the persistence of faint polishing marks in the implanted samples suggests that the damage remains subcritical and does not reach the threshold for total amorphization. In fully amorphized regions, saturated swelling can erase all surface topography, including polishing marks [39,40]. Therefore, the partial retention of these features indicates a moderate level of disorder, likely confined to long-range defect structures which is consistent with the earlier Raman analysis showing broadened but unshifted LO modes.

Upon annealing at elevated temperatures, as illustrated in Fig. 4 (c–e), the surface undergoes further transformation. Grain boundaries become increasingly visible, appearing as distinct linear or polygonal features that intersect the surface. Meanwhile, the polishing marks continue to fade and become increasingly indistinct. This evolution in surface morphology suggests a thermally driven atomic rearrangement process. A plausible mechanism for this behavior is the migration of surface atoms away from higher-energy regions such as those associated with residual polishing damage towards energetically more favorable sites like grain boundaries. This process reduces overall surface free energy and promotes the formation of a more thermodynamically stable microstructure. The emergence of grain boundary features after annealing also implies partial recovery and reorganization of the implanted region. As defects are annealed out, grain boundaries that were previously hidden beneath a disordered or damaged layer may become exposed or enhanced in contrast. This observation further supports the conclusion drawn from the Raman and FWHM data that annealing facilitates structural recovery, though not to the extent of completely restoring the virgin lattice.

Fig. 5 shows SEM micrographs of triple-implanted SiC samples before and after annealing at temperatures of 1100 °C, 1200 °C, and 1300 °C. As shown in Fig. 5(a), the triple implanted sample surface exhibits numerous irregular structures not observed in either the un-implanted or dual-implanted SiC samples. When compared to the dual-implanted, which lacks these features, it is evident that these irregular surface morphologies (in triple implanted samples) are associated with the presence of implanted He. These irregular structures are consistent with the formation of helium-induced blisters or exfoliated holes, as previously reported in our earlier studies [21,22]. He implantation is well known to cause sub-surface bubble formation, which can coalesce under thermal treatment to form surface blisters or even result in exfoliation. These observations are in agreement with the findings of Mokgadi et al. [22], who reported that He -induced surface degradation in SiC depends strongly on both the implantation and annealing temperature. Notably, in their study, no blisters were observed in co-implanted SiC (with Sr and He) at room temperature. In contrast, in our work He was implanted at 350 °C, at this temperature He mobility increases, promoting bubbles nucleation and growth. Furthermore, Mokgadi et al. [22] observed the onset of blister or hole formation only after annealing at 1000 °C. Similarly, in the current study, annealing of the triple-implanted samples at elevated temperatures (1100–1300 °C) resulted in a clear increase in both the number and apparent size of surface irregularities, as illustrated in Fig. 5(b–d). This supports the role of high-temperature annealing in promoting He diffusion, coalescence of He-vacancy clusters, and subsequent blisters growth or exfoliation. In

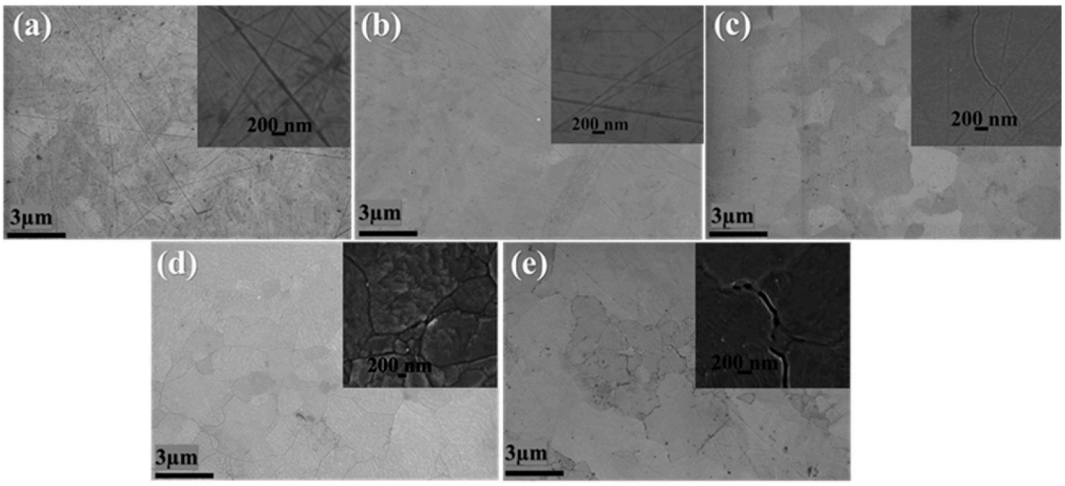

Fig. 4. SEM micrographs of SiC: (a) before implantation, (b) after dual implantation, dual implanted samples then annealed at (c) 1100 °C, (d) 1200 °C, and (e) 1300 °C for 5 h. High-magnification micrographs were also incorporated.

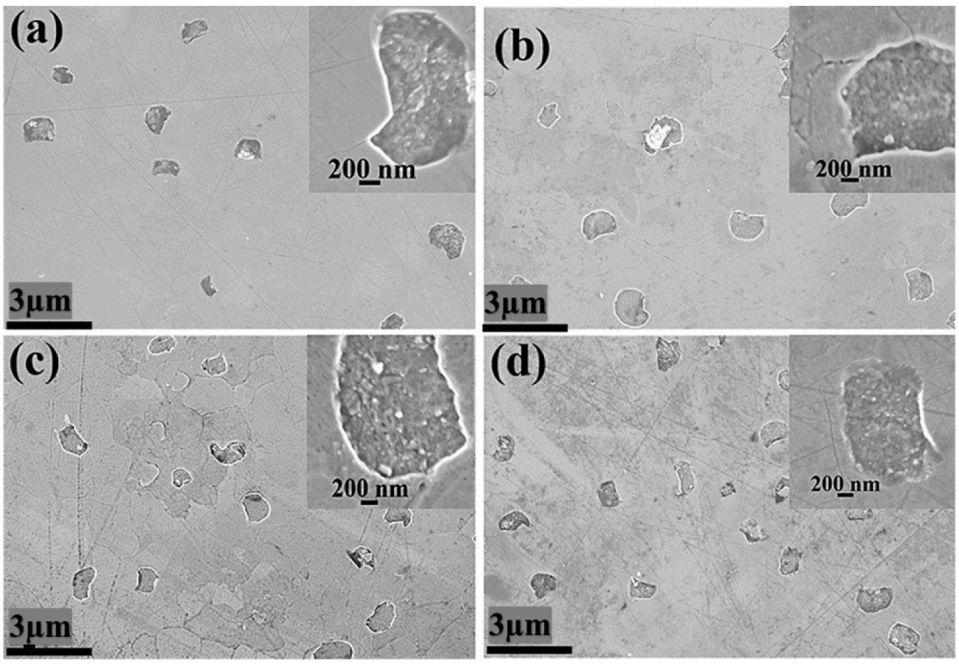

Fig. 5. SEM micrographs of triple implanted SiC before (a) and after annealing at (b) 1100 °C; (c) 1200 °C, and (d) 1300 °C for 5 h. High-magnification micrographs are also incorporated.

addition to the development of these blisters or holes, annealing also leads to the emergence of polishing marks and grain boundaries. The visibility of polishing marks suggests partial relaxation of the surface structure, while the pronounced appearance of grain boundaries indicates suggests some recovery from radiation damage in the implanted sample, consistent with the Raman data presented in Fig. 3(b). The coexistence of recrystallized grains and He-induced surface degradation underscores the complex interplay between defect recovery and He-induced damage during thermal treatment. However, it is important to note that traditional SEM imaging alone cannot provide information about the vertical dimension (depth or height) of He-induced surface features. While SEM effectively highlights the lateral distribution and morphology of surface defects, quantitative analysis of blister height or hole depth requires higher resolution, three-dimensional surface profiling techniques. Accordingly, AFM was employed to assess the depth and topographical dimensions of these features, providing a more complete understanding of helium-induced surface evolution.

Fig. 6 shows atomic force microscopy (AFM) micrographs of triple-implanted SiC samples before and after annealing, alongside corresponding line profile analyses used to quantify the vertical dimensions of surface features such as blisters and holes. The black lines shown in the AFM image mark the path used for extracting height and depth profiles. The AFM data complement the SEM observations shown in Fig. 5, offering critical height and depth measurements that are not accessible via SEM alone. In Fig. 6(a), the as-implanted triple sample reveals the presence of both He blisters and holes on the surface. Line scans across representative features indicate that He blisters exhibit an average height of approximately 70 nm, while the depth of the holes reaches 120 nm. These features are characteristic of He-related surface damage and are attributed to the sub-surface accumulation of He gas, which coalesces to form pressurized bubbles. As these bubbles grow, they can either protrude from the surface as blisters or rupture to form craters or holes.

Following annealing at various temperatures (as seen in Fig. 6(b–d)), a clear transformation in surface morphology is observed. The number of helium blisters decreases, whereas the number of holes increases with increasing annealing temperature. This trend aligns well with the SEM observations discussed previously (Fig. 5), supporting the hypothesis that elevated temperatures promote He bubbles rupture and exfoliation, transitioning blistered regions into open surface craters. This transformation is thermodynamically driven, as annealing facilitates He mobility and bubble coalescence, eventually leading to surface failure.

Interestingly, the average depth of the holes remains consistent at approximately 120 nm, regardless of the annealing temperature. This suggests that the vertical extent of He-induced surface damage is established during implantation and remains largely unchanged during post-implantation thermal processing. The constancy of holes depth also implies that He bubbles rupture primarily affects the surface layer, rather than driving deeper structural changes within the SiC matrix. The stark contrast in surface evolution between dual and triple implanted samples (highlighted in Figs. 4–6) further underscores the significant role of He in modifying the surface morphology of SiC. Dual-implanted samples exhibit smoother surfaces with the emergence of grain boundaries after annealing, whereas triple-implanted samples develop roughened surfaces populated by blisters and holes. Surface roughness, blistering, and the presence of open surface features can alter diffusion paths, surface binding energies, and trap densities, potentially leading to different migration behaviors of implanted species (Ag and Sr) between dual and triple samples. To investigate this hypothesis, RBS analysis was conducted to monitor the post-annealing migration behavior of Ag and Sr in both dual and triple implanted samples.

Fig. 7 shows the depth profiles of Ag and Sr in both dual and triple implanted SiC samples before and after annealing at various temperatures, obtained from RBS spectra (not shown). As shown in Fig. 7(a), the depth profile of the implanted Ag and Sr in the dual-implanted samples is asymmetric before annealing. This asymmetry likely arises due to the overlap between the implanted Ag and Sr ions, resulting in a non-uniform distribution of these elements within the material. Additionally, this asymmetric profile could be influenced by the formation of Ag precipitates or clusters, a phenomenon previously observed in our study on co-implanted SiC samples under similar conditions [17,29]. The clustering or precipitation of Ag in particular can cause localized high concentrations of the element, which would distort the expected uniformity of the depth profile [17]. Moreover, the implantation of He in the triple-implanted SiC samples did not significantly alter the depth profiles of Ag and Sr, as shown in Fig. 7(b). However, annealing at

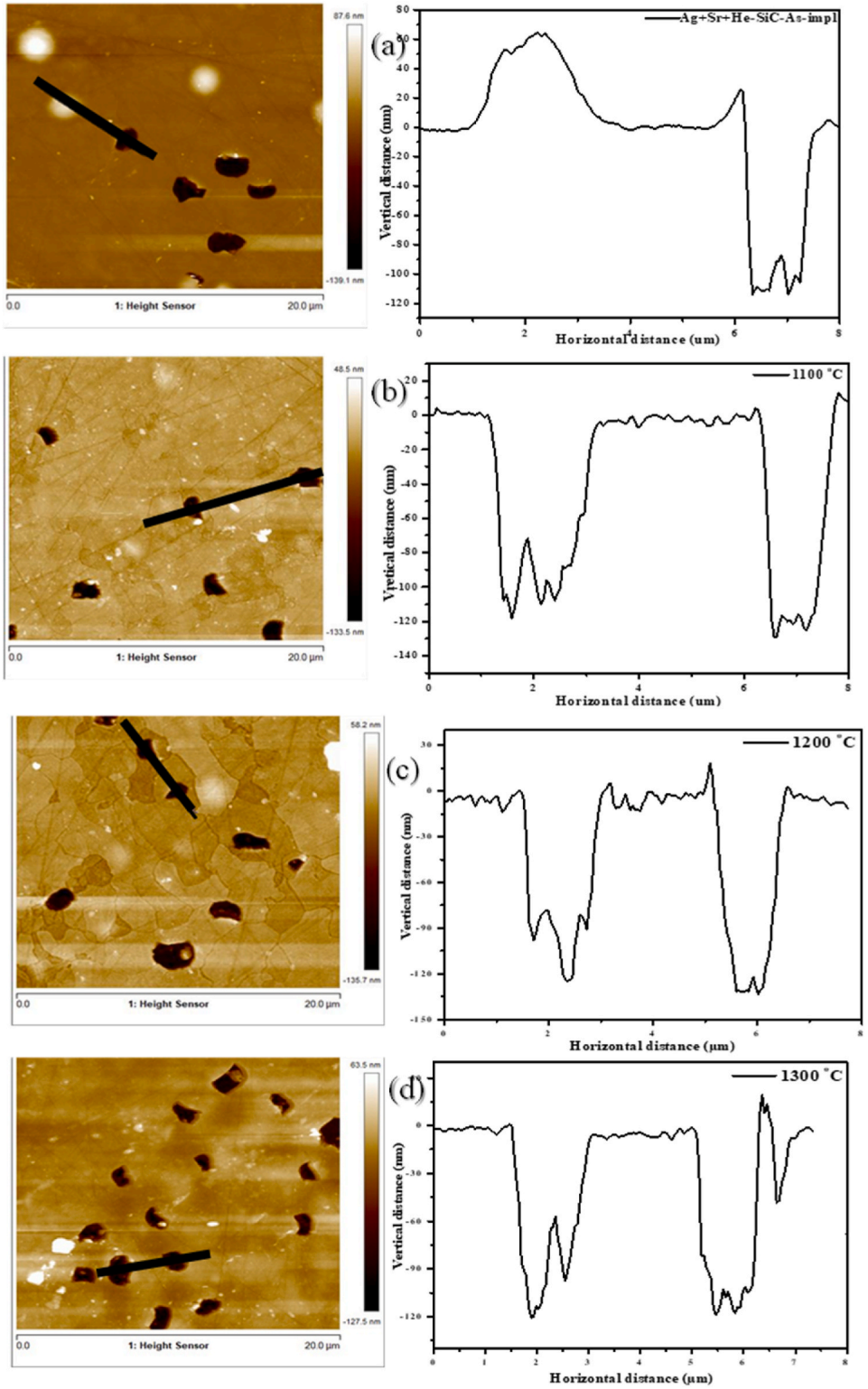

Fig. 6. AFM micrograms of triple implanted samples before, and after isochronal annealing at (b) 1100 °C, (c) 1200 °C, (d), 1300 °C for 5 h. They are shown along with their corresponding line profiles.

1100 °C caused a distinct change in the depth profiles of Ag and Sr in the triple implanted samples. Specifically, the peak height of the Ag and Sr profiles decreased, while the profile itself remained asymmetrical. Furthermore, a loss of Ag and Sr was observed in the near-surface region (about 50 nm below the surface), indicating that a substantial amount of these elements had migrated or evaporated from the surface. The loss of Ag and Sr (around 20 % from their initial concertation – see Fig. 8) can be attributed to the presence of holes or blisters on the surface, as shown in Fig. 6, which could act as diffusion pathways for Ag and Sr. The holes provided a route for the sublimation of these elements, particularly given that the annealing temperature of 1100 °C exceeds the melting points of both Ag and Sr. In contrast to the triple-implanted samples, no similar loss of Ag and Sr was observed in the dual-implanted SiC samples after annealing at 1100 °C. This indicates that the surface features and

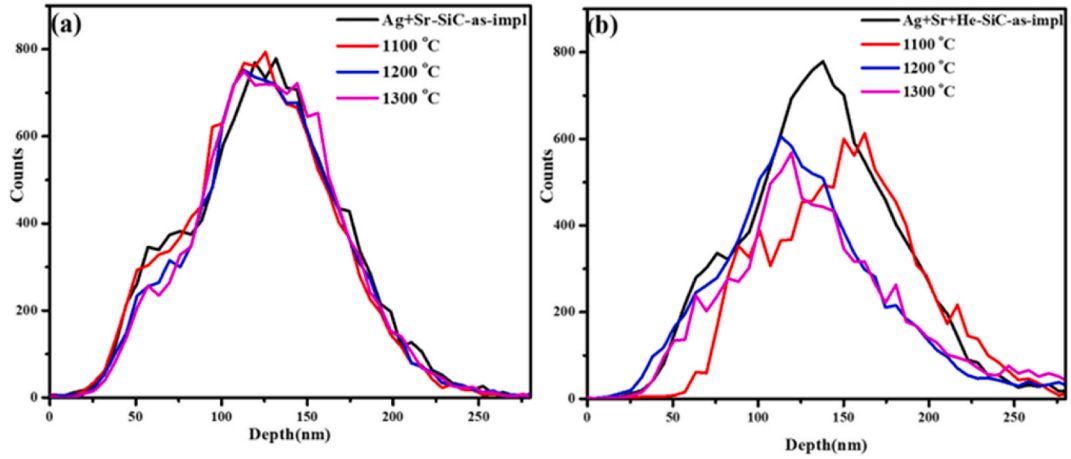

Fig. 7. Depth profiles of Ag and Sr in the (a) dual and (b) triple implanted samples before and after annealing at 1100, 1200 and 1300 °C.

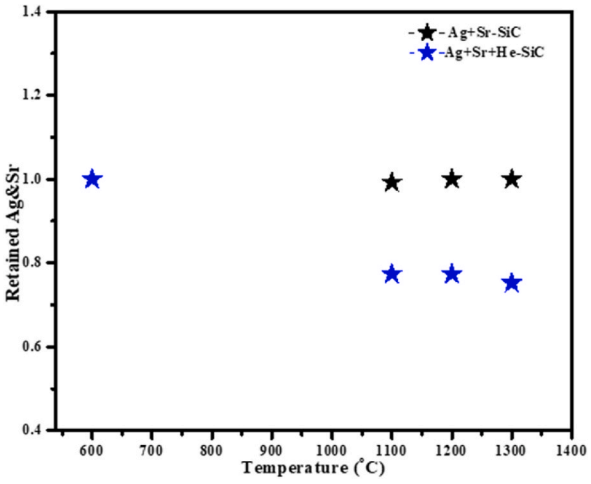

Fig. 8. The retained Ag and Sr atoms in dual (black stars) and triple (blue stars) implanted samples before and after annealing. (For interpretation of the references to colour in this figure legend, the reader is referred to the Web version of this article.)

defects induced by He implantation in the triple-implanted samples play a crucial role in the loss of implanted species.

Further analysis of the retained ratios of Ag and Sr in both dual and triple implanted samples after annealing at 1100, 1200, and 1300 °C is presented in Fig. 8. The retained ratios were taken as the ratio of the area of Ag and Sr counts after annealing to those of the as-implanted samples. Notably, no loss of Ag and Sr was observed in the dual-implanted samples after annealing up to 1300 °C, suggesting that these samples experienced minimal migration or sublimation of the implanted species. This is accompanied by only slight changes in the depth profiles of the dual-implanted samples after annealing up to 1300 °C, indicating limited migration of Ag and Sr in the absence of major surface defects (such as voids). In contrast, the triple-implanted samples exhibited significant changes in the depth profiles after annealing at 1200 and 1300 °C, with the profiles shifting toward the surface. Importantly, no further loss of Ag and Sr was observed at these higher annealing temperatures (1200 and 1300 °C). This can be explained by the fact that annealing at 1100 °C leads to the formation of volatile species from Ag and Sr within the holes (i.e., it is around 120 nm deep, so it is close to the projected range of implanted species), which can escape into the vacuum chamber. However, annealing at higher temperatures (1200 and 1300 °C) facilitates the migration of Ag and Sr atoms from deeper regions towards the surface, even in the presence of surface defects. This suggests that defects in the SiC lattice, which are more abundant in the triple-implanted samples, as evidenced by the Raman results in Fig. 2, can act as diffusion pathways that assist in the migration of implanted species towards the surface.

Overall, the results indicated that He implantation in triple-implanted SiC samples significantly alters the migration and loss behavior of Ag and Sr during annealing. The presence of surface defects, such as He-induced holes and blisters, facilitates the sublimation of these elements at lower annealing temperatures, whereas higher temperatures promote the migration of Ag and Sr atoms without further loss. These findings emphasize the complex role of implantation-induced defects in mediating the behavior of implanted species during thermal treatments. The presence of defects in SiC has been shown to facilitate the migration of Ag and Sr [11,13,17,29].

Fig. 9 shows high-angle annular dark-field (HAADF) scanning transmission electron microscopy (STEM) micrographs of dual- and triple-implanted SiC samples. The double white arrows in Fig. 9 show damaged layers in the dual and triple implanted samples, while the single arrow shows Ag clusters within the implanted region. The damaged layers thicknesses in the dual and triple implanted samples were 230 nm and 272 nm, respectively. The increased thickness in the triple-implanted sample suggests that He implantation contributed to additional damage, probably due to the higher overall displacement damage predicted by SRIM simulations (Fig. 1). Additionally, swelling in the triple-implanted SiC, which is attributed to the formation of He-induced bubbles, as reported in Ref. [29], may also contribute to the observed thickness increase. Ag clusters were also observed in the dual-implanted samples, which can be explained by the role of Sr in promoting the aggregation of Ag atoms in SiC, as discussed in Ref. [17].

Figs. 10 and 11 present HAADF STEM micrographs of the dual- and triple-implanted SiC samples, respectively, following post-implantation annealing at 1100 °C and 1200 °C. These images are accompanied by EDX elemental mapping to provide spatial distribution information for the implanted species. Selected area electron diffraction (SAED) patterns, taken from the damaged regions of both samples, are also included in these figures. In each micrograph, the red arrow denotes the surface of the sample, while the white double-headed arrow indicates the thickness of the damaged layer within the SiC substrate.

Prior to annealing, the thicknesses of the damaged layers in both dual-implanted and triple-implanted samples exceeded 200 nm – see Fig. 9. However, significant changes were observed after thermal annealing. As shown in Fig. 10, the damaged layer in the dual-implanted samples decreased in thickness to 185 nm and 163 nm after annealing at 1100 °C and 1200 °C, respectively. This reduction is attributed to partial recrystallization and epitaxial regrowth at the interface between the damaged layer and the underlying crystalline SiC substrate. The thermal

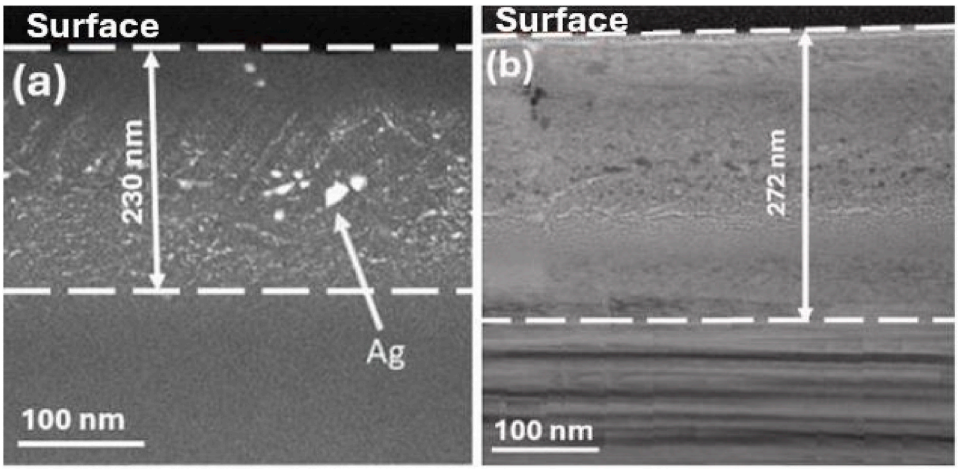

Fig. 9. *High-angle annular dark-field (HAADF) scanning transmission electron microscopy (STEM) micrograph of the (a) dual (Ag + Sr-SiC) and (b) triple implanted samples (Ag + Sr + He-SiC–SiC) before annealing.*

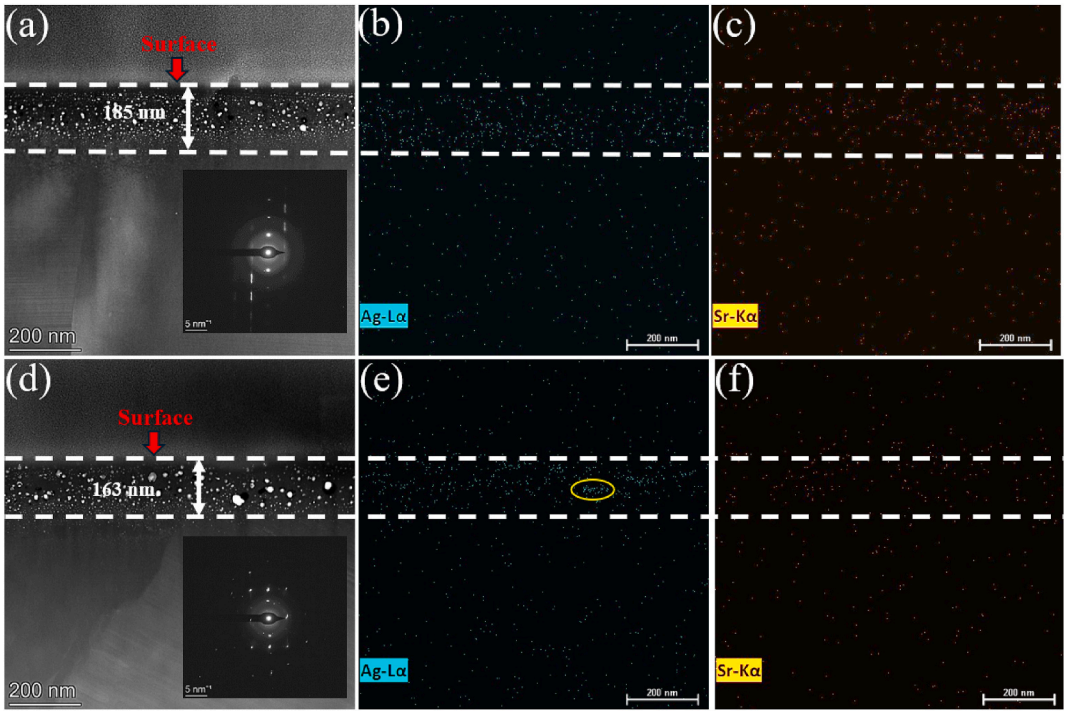

Fig. 10. *High-angle annular dark-field (HAADF) scanning transmission electron microscopy (STEM) micrograph of the dual implanted samples (Ag + Sr–SiC) after annealing at (a) 1100 °C and (d) 1200 °C, with their respective SAD pattern taken from the damaged SiC. The EDX mapping of Ag atoms in implanted region after annealing at 1100 and 1200 °C are shown in (b) and (e) respectively, while (c) and (f) show the EDX mapping of Sr atoms in implanted region after annealing at 1100 and 1200 °C respectively.*

energy provided during annealing facilitates atomic mobility, allowing damaged regions to recover and re-align with the crystalline lattice structure of the substrate.

In contrast, the triple-implanted samples showed no significant change in the thickness of the damaged layer after annealing under the same conditions, as observed in Fig. 11 (a) and (d). This suggests that the additional implanted species in this case, helium plays a critical role in hindering the recrystallization process. He is known to form nanoscale bubbles during annealing, which can exert pressure and create internal defects that stabilize the damaged structure, preventing regrowth. These findings are consistent with earlier studies, such as that of [23], where Sr and He ions were co-implanted into SiC at elevated temperatures and subsequently annealed up to 1300 °C. Despite the high annealing temperature, no significant reduction in the damaged layer was observed in those co-implanted samples. Instead, the primary effects noted were helium bubble formation and evidence of Sr migration, further highlighting the disruptive influence of helium on structural recovery.

By directly comparing Fig. 10 (a, d) with Fig. 11(a–d), the inhibitory effect of He on epitaxial regrowth becomes evident. While the dual-implanted samples benefit from enhanced lattice recovery and damage reduction with increased annealing temperature, the triple-implanted samples remain structurally stagnant, despite being subjected to the same thermal treatment. This points to a strong interaction between helium and the SiC matrix that impedes healing of the implantation-induced damage.

Furthermore, the SAED patterns provide additional insights into the recrystallization behavior. In Fig. 10(a) and (d), the patterns from the dual-implanted samples exhibit refined and sharper diffraction rings

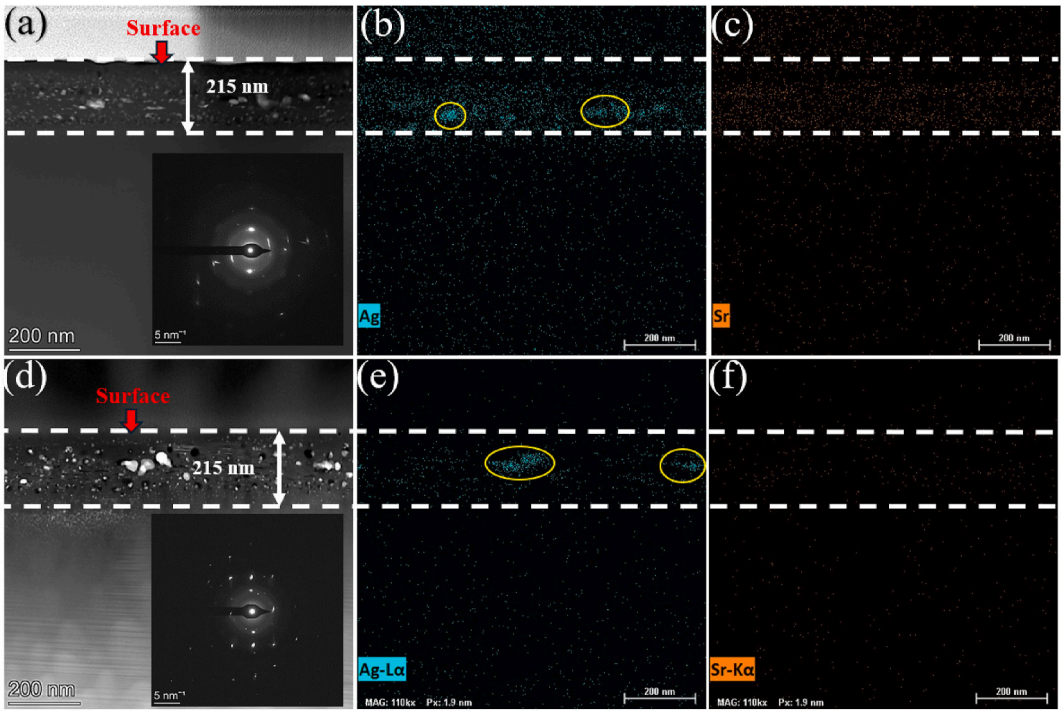

Fig. 11. *High-angle annular dark-field (HAADF) scanning transmission electron microscopy (STEM) micrograph of the triple implanted samples (Ag + Sr + He-SiC–SiC) after annealing at (a) 1100 °C and (d) 1200 °C, with their respective SAD pattern taken from the damaged SiC. The EDX mapping of Ag atoms in implanted region after annealing at 1100 and 1200 °C are shown in (b) and (e) respectively, while (c) and (f) show the EDX mapping of Sr atoms in implanted region after annealing at 1100 and 1200 °C respectively.*

after annealing at 1200 °C, indicating improved crystallinity and the re-establishment of the SiC lattice. This trend suggests that higher annealing temperatures promote greater atomic mobility and lattice recovery in the absence of helium. A similar sharpening of SAED rings is observed in Fig. 11(a) and (d) for the triple-implanted samples, though this occurs without any accompanying reduction in damage layer thickness. This implies that while local ordering and recrystallization may take place, they are confined within a region still surrounded by structurally compromised or helium-stabilized amorphous zones.

These microscopic observations are corroborated by the Raman spectroscopy results shown in Fig. 2. There, an increase in the longitudinal optical (LO) phonon peak intensity is observed after annealing at 1200 °C, which is a strong indicator of recrystallization and improved structural order in the SiC lattice. This agreement between microstructural (STEM/SAED) and spectroscopic (Raman) data reinforces the conclusion that dual implantation, in the absence of helium, allows for more effective thermal recovery of the damaged SiC structure, whereas the presence of helium impedes this process.

In the HAADF STEM micrographs, contrast variations directly relate to the atomic number (Z) of elements present: bright regions indicate heavy elements with high Z-values, such as Ag and Sr, whereas darker regions signify either lighter elements, like He, or structural defects such as cavities and dislocations. As observed in Fig. 11, the presence of dark regions may correspond to helium bubbles or cavities formed during implantation, as supported by our previous findings [21]. In contrast, the brighter regions are indicative of heavy-element clusters, specifically Ag or Sr.

Figs. 10 and 11 (b, c, e, and f) present EDX elemental maps of Ag and Sr distributions in the dual- and triple-implanted SiC samples after annealing at 1100 °C and 1200 °C. While Sr clusters are not distinctly visible in either figure, likely due to their smaller size and lower cohesive energy Ag clusters are clearly observable. These are highlighted using yellow circles and ovals in the micrographs. The visibility of Ag clusters is consistent with known material behavior: impurity atoms often aggregate into clusters or particles within the host lattice, driven by cohesive interactions between atoms [41]. Notably, Ag has a significantly higher cohesive energy (2.96 eV/atom) compared to Sr (1.70 eV/atom) [42], enabling the formation of larger, more detectable Ag clusters. This explains why Ag clusters are clearly seen in both dual and triple implanted samples, whereas Sr clusters are either absent or below the resolution threshold of the EDX system.

Interestingly, the size and distribution of Ag clusters differ markedly between the dual and triple implanted samples. In the triple implanted samples (see Fig. 11 (b) and (e)), Ag clusters are substantially larger than those observed in the dual implanted counterparts (Fig. 10 (b) and (e)), despite identical annealing conditions. This enhanced clustering can be attributed to the presence of He in the triple implanted samples. He tends to form bubbles or cavities during annealing, which can act as nucleation sites or traps for Ag atoms. These He-stabilized voids facilitate Ag accumulation, leading to the formation of larger clusters [29].

Further insights into the redistribution of Ag during annealing can be drawn from the spatial positioning of the clusters. After annealing at 1100 °C, Ag clusters in the triple implanted samples predominantly appear at the bottom of the damaged layer, with no significant clustering near the surface (Fig. 11(b)). This observation aligns with depth profiling results (see Fig. 7(b)), which show a depletion of Ag and Sr in the near-surface region, likely due to sublimation through deep surface voids. However, after annealing at 1200 °C, Ag clusters are found much closer to the surface (Fig. 11(e)), correlating with RBS data that indicates a shift in the depth profiles of Ag and Sr toward the surface. The enhanced Ag and Sr migration toward the surface at 1200 °C is likely driven by increased atomic mobility and exacerbated by the presence of crystal defects in the triple implanted samples, which act as diffusion pathways as confirmed by the defect analysis in Figs. 1 and 2.

Fig. 12 shows HAADF STEM micrographs of the dual- and triple-implanted SiC samples after annealing at 1300 °C. SAED patterns taken from the damaged regions of both samples are also included in Fig. 12. The thickness of the damaged layer has decreased to 140 nm and

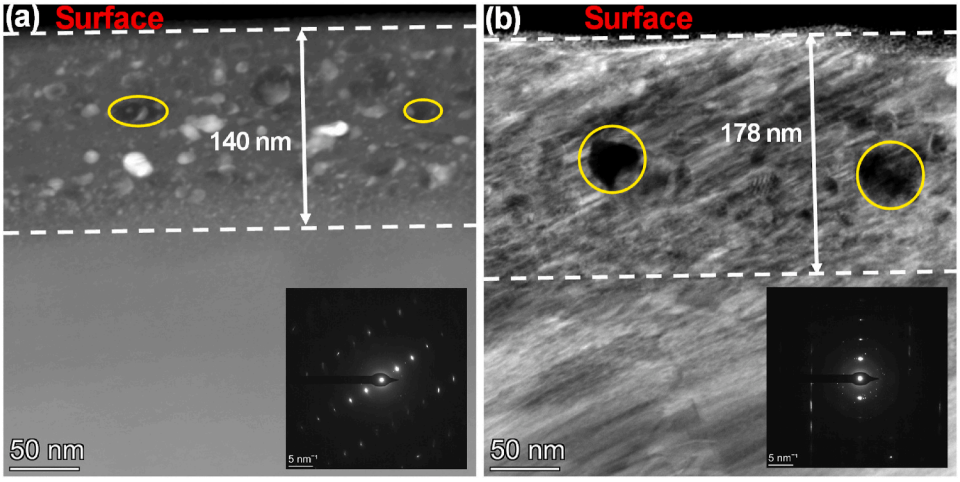

Fig. 12. *High-angle annular dark-field (HAADF) scanning transmission electron microscopy (STEM) micrograph of the (a) dual (Ag + Sr-SiC) and (b) triple implanted samples (Ag + Sr + He-SiC–SiC) after annealing at 1300 °C, with their respective SAED pattern taken from the damaged SiC. The yellow circles and ovals show the Ag and Sr clusters.* (For interpretation of the references to colour in this figure legend, the reader is referred to the Web version of this article.)

178 nm in dual and triple implanted samples respectively, all annealed at 1300 °C. The triple implanted samples still retained a thicker damaged layer and larger Ag and Sr clusters as shown by the yellow circles in Fig. 12 (b). This can be attributed to the presence of He-induced cavities which facilitate the formation of Ag and Sr clusters within the damaged layer in the triple implanted samples. Moreover, from the SAED patterns, dual implanted samples showed more structural recovery than triple implanted samples, all annealed at 1300 °C. This is in good agreement with Raman results which showed a narrower FWHM of the LO peak in dual implanted samples as compared to triple implanted samples (see Fig. 4), all annealed at 1300 °C, indicating more recovery in dual implanted samples. This was attributed to the formation of graphite crystals and He bubbles in the triple implanted samples which hindered the recovery process.

The current findings also show a significant loss of Ag and Sr after annealing at 1100 °C, when compared to our previous study [29], where Ag, Sr, and He were implanted under similar conditions and annealed at 1000 °C for 5 h. Two main factors likely explain this discrepancy. First, the higher annealing temperature used in the present study increases the diffusion and surface migration of implanted species, resulting in greater volatilization and loss. Second, structural differences between the samples also play a crucial role. After annealing at 1000 °C, surface voids were relatively narrow (approximately 0.5 μm in diameter), whereas much larger voids (exceeding 1 μm) formed after annealing at 1100 °C in the triple implanted samples, as shown in Fig. 6(b). These larger voids likely facilitated the sublimation of Ag and Sr atoms, thereby contributing to the observed reduction in their concentrations post-annealing, as evidenced by the compositional profiles in Fig. 8.

4. Conclusion

In this study a comprehensive analysis of the structural and compositional evolution of SiC subjected to dual (Ag + Sr-SiC) and triple (Ag + Sr + He-SiC) implantation was conducted before and after annealing at 1100, 1200 and 1300 °C. The combined use of Raman spectroscopy, SEM, AFM, RBS, HAADF-STEM, SAED, and EDX techniques provided deep insights into the damage mechanisms, recovery processes, and migration behavior of implanted species under varying thermal conditions.

The Raman spectra of the as-implanted samples demonstrated a substantial reduction in the intensity of the characteristic SiC phonon modes, accompanied by the emergence of broad bands associated with the formation of Si–Si and C–C homonuclear bonds. This confirms that ion implantation introduces significant lattice disorder, though complete amorphization was avoided due to implantation at elevated temperatures (above the critical amorphization threshold of ~300 °C). Upon annealing, the dual-implanted samples showed considerable structural recovery, as evidenced by the re-emergence and sharpening of TO and LO phonon peaks, reduction in LO mode FWHM, and partial recrystallization observed in STEM and SAED. SEM and AFM imaging also revealed surface smoothening, grain boundary emergence, and the retention of some polishing marks, indicating moderate but effective lattice healing in the dual implanted samples.

In contrast, triple-implanted samples, containing helium in addition to Ag and Sr, exhibited more complex and less favorable recovery behavior. Raman data revealed the formation of D and G bands after He implantation and annealing, indicating localized graphitization and the formation of carbon-rich phases not observed in dual-implanted samples. The presence of helium strongly influenced surface morphology, leading to the formation of blisters and holes through helium bubble growth and rupture. SEM and AFM confirmed the progressive transformation of blisters into open craters at higher annealing temperatures, with depth profiling indicating that these voids facilitated the sublimation of Ag and Sr, especially at 1100 °C. Notably, despite the presence of local recrystallization signatures (e.g., sharpening of SAED rings), the overall thickness of the damaged layer in triple-implanted samples remained unchanged after annealing up to 1200 °C, in stark contrast to the dual-implanted samples, which exhibited measurable thinning of the damaged region after annealing under the same conditions. This demonstrates the inhibitory effect of helium on epitaxial regrowth and defect recovery.

Additionally, STEM and EDX analyses revealed larger and more Ag clusters in triple-implanted samples compared to their dual-implanted counterparts. These clusters are believed to form due to helium-stabilized voids acting as nucleation sites, which not only impede recrystallization but also promote aggregation of heavy implanted species. The differential mobility and clustering behavior of Ag and Sr were further explained by their respective cohesive energies and the defect pathways facilitated by helium-induced structural damage.

Taken together, these findings demonstrate that helium plays a dual and paradoxical role in ion-implanted SiC: while it can promote some localized recrystallization and phase transformation (e.g., graphitization), its dominant effect is to inhibit long-range structural recovery, promote surface degradation, and alter the redistribution and retention of implanted metallic species. Dual implantation, by contrast, allows for more controlled defect healing and species retention under thermal treatment, making it more favorable for applications requiring high structural stability and chemical containment. Therefore, the presence

of helium introduces a critical trade-off between defect engineering and structural recovery in ion-modified SiC. Considering the effect of He on the migration behavior of Ag and Sr in the SiC layer under accident conditions, the findings in this study are crucial for understanding the efficiency of TRISO particles.

CRediT authorship contribution statement

G. Ntshobeni: Writing – original draft, Investigation, Formal analysis, Conceptualization. **Z.A.Y. Abdalla:** Writing – review & editing, Investigation, Formal analysis, Supervision. **H.A.A. Abdelbagi:** Writing – review & editing, Investigation, Formal analysis. **A. Sohatsky:** Resources, Data curation. **T. Nguyen:** Resources, Data curation. **E.G. Njoroge:** Writing – review & editing, Investigation, Formal analysis. **V. A. Skuratov:** Resources, Data curation. **M. Mlambo:** Writing – review & editing, Investigation, Formal analysis. **T.T. Hlatshwayo:** Writing – review & editing, Supervision, Resources, Investigation, Formal analysis, Conceptualization.

Declaration of competing interest

The authors declare that they have no known competing financial interests or personal relationships that could have appeared to influence the work reported in this paper.

Acknowledgements

Financial support by the National Research Foundation of South Africa (Grant numbers: 30308881411, 2204072593 and 141358) is gratefully acknowledged.

References

[1] D.A. Petti, P.A. Demkowicz, J.T. Maki, R.R. Hobbins, TRISO-Coated particle fuel performance, Compr. Nuclear Mater. 3 (2012) 151–213.
[2] J.B. Malherbe, E. Friedland, N.G. van der Berg, Ion beam analysis of materials in the PBMR reactor, Nucl. Instrum. Methods Phys. Res. Sect. B Beam Interact. Mater. Atoms 266 (2008) 1373–1377.
[3] J.B. Malherbe, Topical Review: diffusion of fission products and radiation damage in SiC, J. Appl. Phys. 46 (2013) 473001.
[4] K. Verfondern, H. Nabielek, J.M. Kendall, Coated particle fuel for high temperature gas cooled reactors, Nucl. Eng. Technol. 39 (2007) 603.
[5] J.B. Malherbe, Diffusion of fission products and radiation damage in SiC, J. Phys. Appl. Phys. 46 (47) (2013) 473001.
[6] TECDOC- 978, Fuel Performance and Fission Product Behaviour in Gas-Cooled Reactors, Tech.Rep, IAEA, Vienna, 1997. https://www.iaea.org/publications/5633/fuel-performance-and-fission-product-behaviour-in-gascooled-reactors.
[7] J.J. Van der Merwe, Evaluation of silver transport through SiC during the German HTR fuel program, J. Nucl. Mater. 395 (2009) 99–111.
[8] P.E. Brown, R.L. Faircloth, Metal fission product behaviour in high temperature reactors-UO_2 coated particle fuel, J. Nucl. Mater. 59 (1976) 29–41.
[9] H. Nabielek, P.E. Brown, P. Offermann, Silver release from coated particle fuel, Nucl. Technol. 35 (1977) 483–493.
[10] R.E. Bullock, Fission-product release during post irradiation annealing of several types of coated fuel particles, J. Nucl. Mater. 125 (1984) 304–319.
[11] E. Friedland, N.G. van der Berg, J.B. Malherbe, E. Wendler, W. Wesch, Influence of radiation damage on strontium and iodine diffusion in silicon carbide, J. Nucl. Mater. 425 (2012) 205–210.
[12] E. Friedland, T. Hlatshwayo, N. Van der Berg, Influence of radiation damage on diffusion of fission products in silicon carbide, Phys. Status Solidi c 10 (2013) 208–215.
[13] E. Friedland, J.B. Malherbe, N.G. Van der Berg, T. Hlatshwayo, A.J. Botha, E. Wendler, W. Wesch, Study of silver diffusion in silicon carbide, J. Nucl. Mater. 389 (2009) 326–331.
[14] T.T. Hlatshwayo, J.B. Malherbe, N.G. Van Der Berg, A.J. Botha, P. Chakraborty, Effect of thermal annealing and neutron irradiation in 6H-SiC implanted with silver at 350 °C and 600 °C, Nucl. Instrum. Methods Phys. Res. Sect. B Beam Interact. Mater. Atoms 273 (2012) 61–64.
[15] T.T. Hlatshwayo, J.B. Malherbe, N.G. Van Der Berg, L.C. Prinsloo, A.J. Botha, E. Wendler, W. Wesch, Annealing of silver implanted 6H–SiC and the diffusion of the silver, Nucl. Instrum. Methods Phys. Res. Sect. B Beam Interact. Mater. Atoms 274 (2012) 120–125.
[16] H.J. MacLean, R.G. Ballinger, Silver ion implantation and annealing in CVD silicon carbide: the effect of temperature on silver migration. Proceeding of High Temperature Reactors, 2004.
[17] T.T. Hlatshwayo, N. Mtshonisi, E.G. Njoroge, M. Mlambo, M. Msimanga, V. A. Skuratov, S.V. Motloung, Effects of Ag and Sr dual ions implanted into SiC, Nucl. Instrum. Methods Phys. Res. Sect. B Beam Interact. Mater. Atoms 472 (2020) 7–13.
[18] H. Neethling, J.H. O'Connell, E.J. Olivier, Palladium assisted silver transport in polycrystalline SiC, Nucl. Eng. Des. 251 (2012) 230–234.
[19] T.T. Hlatshwayo, N.G. Van Der Berg, M. Msimanga, J.B. Malherbe, R.J. Kuhudzai, Iodine assisted retainment of implanted silver in 6H-SiC at high temperatures, Nucl. Instrum. Methods Phys. Res. Sect. B Beam Interact. Mater. Atoms 334 (2014) 101–105.
[20] J.H. O'Connell, J.H. Neethling, Palladium and ruthenium supported silver migration in 3C–silicon carbide, J. Nucl. Mater. 456 (2015) 436–441.
[21] S.Z. Mtsi, A. Sohatsky, Z.A.Y. Abdalla, E.G. Njoroge, V.A. Skuratov, S.V. Motloung, T.T. Hlatshwayo, Effects of helium (He) bubbles and annealing on the structural evolution and migration behavior of silver (Ag) implanted into polycrystalline SiC at 350 °C, Vacuum 218 (2023) 112621.
[22] T. Mokgadi, Z. Abdalla, H. Abdelbagi, M. Msimanga, C. Maepa, V. Skuratov, T. Hlatshwayo, Helium and strontium co-implantation into SiC at room temperature and isochronal annealing: structural evolution of SiC and migration behaviour of strontium, Mater. Chem. Phys. 294 (2023) 126998.
[23] T.T. Hlatshwayo, T.F. Mokgadi, S.S. Ntshangase, Z.A.Y. Abdalla, E.G. Njoroge, T. Nguyen, V.A. Skuratov, The effects of co-implanting strontium (Sr) and helium (He) into SiC at temperatures exceeding the critical amorphization temperature and annealing above 1000 °C, Ceram. Int. (2025).
[24] T.F. Mokgadi, Z.A.Y. Abdalla, M. Madhuku, E.G. Njoroge, M. Mlambo, P. Mdluli, T. T. Hlatshwayo, The influence of helium-induced defects on the migration of strontium implanted into SiC above critical amorphization temperature, Front. Mater. 10 (2023) 1192989.
[25] T.T. Hlatshwayo, T.F. Mokgadi, A. Sohatsky, Z.A.Y. Abdalla, V.A. Skuratov, E. G. Njoroge, M. Mlambo, The migration behaviour of strontium co-implanted with helium into SiC at room temperature and annealed at temperatures above 1000 °C, Vacuum 230 (2024) 113676.
[26] T.T. Hlatshwayo, C.E. Maepa, M. Msimanga, M. Mlambo, E.G. Njoroge, V. A. Skuratov, J.B. Malherbe, Helium assisted migration of silver implanted into SiC, Vacuum 183 (2021) 109865.
[27] C. Chen, T. Wang, H. Zang, F. Liu, P. Zhou, T. Shi, Y. Zhu, Unraveling interaction mechanisms of Kr cavities with Ag in irradiated silicon carbide under high temperatures, Nucl. Instrum. Methods Phys. Res. Sect. B Beam Interact. Mater. Atoms 563 (2025) 165697.
[28] J. Sun, B.S. Li, Y.W. You, J. Hou, Y. Xu, C.S. Liu, Z.G. Wang, The stability of vacancy clusters and their effect on helium behaviors in 3C-SiC, J. Nucl. Mater. 503 (2018) 271–278.
[29] G. Ntshobeni, Z.A.Y. Abdalla, T.F. Mokgadi, M. Mlambo, E.G. Njoroge, M. Msimanga, A. Sohatsky, V.A. Skuratov, T.T. Hlatshwayo, The effects of helium, strontium, and silver triple ions implanted into SiC, Heliyon 9 (2023) e20877.
[30] K.J. Stevenson, Review of OriginPro 8.5, J. Am. Chem. Soc. 133 (2011) 5621.
[31] NanoScope Software 6.13 User Guide, V.I.I, Version; Veeco Instruments Inc., Plainview, NY, USA, 2004.
[32] AFM resource library-agilent technology. http://www.afmuniversity.org. (Accessed 28 April 2024).
[33] J.F. Ziegler, M.D. Ziegler, J.P. Biersack, SRIM–The stopping and range of ions in matter, (2010), Nucl. Instrum. Methods Phys. Res. Sect. B Beam Interact. Mater. Atoms 268 (2010) 1818–1823.
[34] W.J. Weber, F. Gao, R. Devanathan, W. Jiang, The efficiency of damage production in silicon carbide, Nucl. Instrum. Methods Phys. Res. Sect. B Beam Interact. Mater. Atoms 218 (2004) 68–73.
[35] C.J. McHargue, J.M. Williams, Ion implantation effects in silicon carbide, Nucl. Instrum. Methods Phys. Res. Sect. B Beam Interact. Mater. Atoms 80 (1993) 889–894.
[36] Z.A.Y. Abdalla, M.Y.A. Ismail, E.G. Njoroge, E. Wendler, J.B. Malherbe, T. T. Hlatshwayo, Effect of heat treatment on the migration behaviour of selenium implanted into polycrystalline SiC, Nucl. Instrum. Methods Phys. Res. Sect. B Beam Interact. Mater. Atoms 487 (2021) 30–37.
[37] J. Wasyluk, T.S. Perova, S.A. Kukushkin, A.V. Osipov, N.A. Feoktistov, S. A. Grudinkin, Raman investigation of different polytypes in SiC thin films grown by solid-gas phase epitaxy on Si (111) and 6H-SiC substrates, Mater. Sci. Forum 645 (2010) 359–362.
[38] S. Lin, Z. Chen, L. Li, C. Yang, Effect of impurities on the Raman scattering of 6H-SiC crystals, Mater. Res. 15 (2012) 833–836.
[39] H.A.A. Abdelbagi, V.A. Skuratov, S.V. Motloung, E.G. Njoroge, M. Mlambo, J. B. Malherbe, T.T. Hlatshwayo, Effect of swift heavy ions irradiation in the migration of silver implanted into polycrystalline SiC, Nucl. Instrum. Methods Phys. Res. Sect. B Beam Interact. Mater. Atoms 461 (2019) 201–209.
[40] H.A.A. Abdelbagi, V.A. Skuratov, S.A. Adeojo, T.M. Mohlala, T.T. Hlatshwayo, J. B. Malherbe, Effect of SHI irradiation and high temperature annealing on the microstructure of SiC implanted with Ag, Nucl. Instrum. Methods Phys. Res. Sect. B Beam Interact. Mater. Atoms 511 (2022) 18–29.
[41] B.E. Husic, D. Schebarchov, D.J. Wales, Impurity effects on solid–solid transitions in atomic clusters, Nanoscale 8 (43) (2016) 18326–18340.
[42] J. Sólyom, Bonding in solids, in: Fundamentals of the Physics of Solids, Volume I: Structure and Dynamics, vol. 1, Springer, 2007, pp. 75–108.